ACS central science

http://pubs.acs.org/journal/acscii

Research Article

Bottlebrush Bridge between Soft Gels and Firm Tissues

Andrew N. Keith, Mohammad Vatankhah-Varnosfaderani, Charles Clair, Farahnaz Fahimipour, Erfan Dashtimoghadam, Abdelaziz Lallam, Michael Sztucki, Dimitri A. Ivanov,* Heyi Liang, Andrey V. Dobrynin,* and Sergei S. Sheiko*

Cite This: *ACS Cent. Sci.* 2020, 6, 413–419

Read Online

ACCESS | Metrics & More | Article Recommendations | Supporting Information

ABSTRACT: Softness and firmness are seemingly incompatible traits that synergize to create the unique soft-yet-firm tactility of living tissues pursued in soft robotics, wearable electronics, and plastic surgery. This dichotomy is particularly pronounced in tissues such as fat that are known to be both ultrasoft and ultrafirm. However, synthetically replicating this mechanical response remains elusive since ubiquitously employed soft gels are unable to concurrently reproduce tissue firmness. We have addressed the tissue challenge through the self-assembly of linear−bottlebrush−linear (LBL) block copolymers into thermoplastic elastomers. This hybrid molecular architecture delivers a hierarchical network organization with a cascade of deformation mechanisms responsible for initially low moduli followed by intense strain-stiffening. By bridging the firmness gap between gels and tissues, we have replicated the mechanics of fat, fetal membrane, spinal cord, and brain tissues. These solvent-free, nonleachable, and tissue-mimetic elastomers also show enhanced biocompatibility as demonstrated by cell proliferation studies, all of which are vital for the safety and longevity of future biomedical devices.

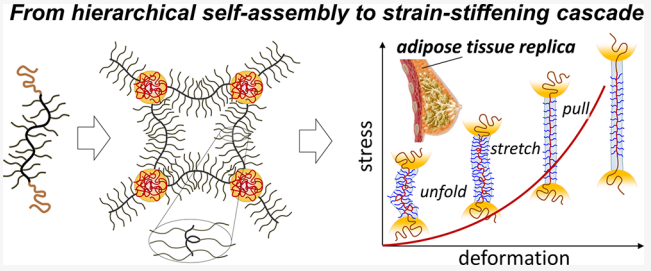

INTRODUCTION

Soft tissues are distinct in possessing an oxymoronic mechanical property combination: they are compliant to the touch yet resistant to deformation, which imbues their characteristic feeling of firmness.[1,2] While initially they are very soft with Young's moduli ranging from $E_0 = 10^3-10^5$ Pa, tissues rapidly stiffen by a factor of 10^2-10^3 within a short interval of strain (Figure 1a).[3−6] This strain-adaptive stiffening represents one of nature's key defense mechanisms that prevents accidental tissue rupture and serves as a benchmark for various industrial[7,8] and biomedical applications.[9−12] Tissue softness is routinely replicated with polymer gels,[13] but gels are limited in their ability to copy nature's strain-stiffening capabilities (Figure 1b) as accentuated by the sharply diverging deformation responses of adipose tissue and a silicone gel utilized in breast implants (Figure 1c). This mechanical mismatch is further exacerbated by both spontaneous[14] and induced[15] solvent migration leading to inadequate performance of engineered devices and unforeseen health risks.[16]

RESULTS AND DISCUSSION

To guide the materials design toward soft tissue firmness, we introduce an equation of state relating true stress σ_{true} with sample uniaxial elongation ratio $\lambda = L/L_0$ from its initial size L_0 to deformed size L as

$$\sigma_{true} = \frac{E}{9}(\lambda^2 - \lambda^{-1})\left(1 + 2\left[1 - \frac{\beta}{3}(\lambda^2 + 2\lambda^{-1})\right]^{-2}\right) \quad (1)$$

which describes the nonlinear elastic response of polymer networks (Figure 1a,b) as a function of two molecular parameters: structural modulus E and strain-stiffening parameter β.[19] The modulus is controlled by the density (ρ_s) and conformation of stress-supporting strands as $E \cong k_B T \rho_s \langle R_{in}^2 \rangle / (b_K R_{max})$, where b_K, $\langle R_{in}^2 \rangle$, and R_{max} are a strand's Kuhn length, mean square end-to-end distance, and contour length. The strain-stiffening curvature (Figure 1c) is determined by potential extensibility of network strands from their initial mean-square end-to-end distance $\langle R_{in}^2 \rangle$ to the corresponding contour length of a fully extended strand as $\beta = \langle R_{in}^2 \rangle / R_{max}^2$ such that $0 < \beta < 1$. For polymer networks with nonlinear responses, the Young's modulus E_0 depends not only on network strands density ($E \sim \rho_s$), but also on their initial conformations ($\beta \sim \langle R_{in}^2 \rangle$) as

$$E_0 = \left.\frac{\partial \sigma_{true}}{\partial \lambda}\right|_{\lambda \to 1} = \frac{E}{3}\left(1 + \frac{2}{(1-\beta)^2}\right) \quad (2)$$

Received: November 25, 2019
Published: January 22, 2020

https://dx.doi.org/10.1021/acscentsci.9b01216
ACS Cent. Sci. 2020, 6, 413−419

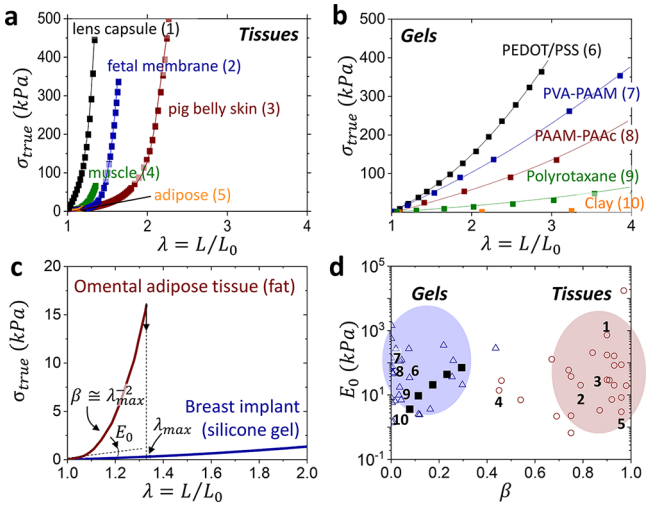

Figure 1. Mechanical mismatch. Stress−elongation curves of assorted (a) biological tissues and (b) polymeric gels, which demonstrate tissue's much stronger stiffening (Tables S1 and S2). Lines guide the reader, while data points represent literature data. (c) Stress−elongation responses of omental adipose tissue and silicone gel extracted from a commercial breast implant display a significant difference in strain-stiffening (β) despite a similarity in the Young's modulus (E_0). (d) An E_0 vs β map partitions polymeric gels (△) and biological tissues (○) as two distinct classes of materials. The β values are obtained by fitting stress−elongation curves with eq 1, whereas E_0 corresponds to the curve slope at $\lambda \rightarrow 1$ (eq 2). The model is successful in fitting the entirety of gel elasticity, but only the elastic portion of tissue response before yielding.[17] Numbers at data points correspond to the stress−elongation curves in (a, b). Bottlebrush elastomers (■) mimic the stress−strain response of gels,[18] but are unable to reach the tissue territory.

Simply, this elastic model provides two parameters observable in stress−elongationplots (Figure 1c): the initial slope or softness (E_0) followed by a curvature or firmness (β), which characterizes resistivity of material to deformation. Respectively, mapping [E_0, β] allows partitioning gels and tissues into two distinct materials classes with similar E_0 yet vastly different β ($\beta_{gel} \ll \beta_{tissue}$) (Figure 1d). The limited firmness of linear-chain polymeric gels ($\beta_{gel} = \beta_{dry}\langle R_{in}^2\rangle_{gel}/\langle R_{in}^2\rangle_{dry} = \beta_{dry}\alpha^{2/3} <$ 0.2) originates both from weak strand extension in as-prepared networks ($\beta_{dry} \cong 0.01$) and an upper bound on their swelling ratio ($\alpha < 100$).[20] For a deeper discussion on the origins and validity of this elastic model, we encourage the reader to pursue prior literature.[19]

Various molecular and macroscopic constructs have endeavored to bridge the *strain-stiffening divide* and replicate tissue firmness ($0.7 < \beta < 1$) in Figure 1b,[17,18,21−26] but as of now, most attempts have fallen short of $\beta > 0.4$, including our earlier studies utilizing solvent-free bottlebrush elastomers (filled squares ■ in Figure 1d).[18]

In this regard, self-assembled networks of linear−bottlebrush−linear (LBL) block copolymers have proven to be a resourceful scaffold given the hierarchical integration of molecular and particulate motifs within each network strand (Figure 2a).[17] On the molecular scale, B-block side chains simultaneously decrease cross-link density and extend network strands promoting both softness and firmness, respectively.[27] Additional strain-stiffening results from strong microphase separation between both the chemically and architecturally distinct blocks forcing further strand extension (R_{in} increase).[28]

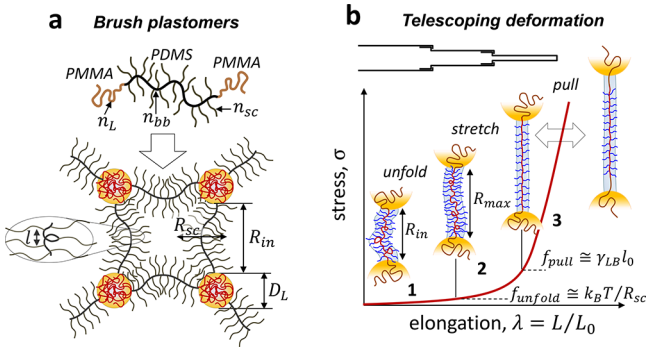

Figure 2. Hierarchical deformation. (a) LBL self-assembly is regulated by molecular (n_{bb}, n_{sc}, n_L) and morphological (R_{sc}, D_L, R_{in}, l) parameters, where *Rsc* - brush radius, D_L - L-block domain diameter, and *l* - distance between neighboring side chains along the bottlebrush contour. (b) The cascade of deformation mechanisms during uniaxial extension of LBL networks: (1) unfolding of bottlebrush filaments limited by $f_{unfold} < k_BT/b_K \cong k_BT/R_{sc} \cong 0.5$ pN (for $n_{sc} = 70$), (2) stretching of backbones inside brush envelops ranging within $k_BT/R_{sc} < f_{stretch} < k_BT/l_0 \cong 20$ *pN*, where $l_0 = 0.25$ nm is the monomer projection length, and (3) pulling linear chains from microdomains creating a new interface between exposed linear block sections and the bottlebrush matrix. The two-head arrow indicates that chain pulling may overlap with backbone stretching. The pulling force is on the order of $f_{pull} \cong \gamma_{LB}l_0 \cong 2.5$ pN, where $\gamma_{LB} \cong 10$ mN is the surface energy of the L−B interface. The actual f_{pull} value may be higher due to kinetic barriers imparted by glassy L-domains.

On a mesoscopic scale, bottlebrush strands behave as flexible filaments that exhibit low bending rigidity and unfold at lower forces followed by stretching of the bottlebrush backbone and concomitant withdrawal of L-blocks from microdomains at higher forces. Critically, L-block microdomains serve as hidden length reservoirs[29] that offset the limited extensibility of the inherently strained brush-like strands while also mitigating uneven stress distributions. This hierarchical organization empowers telescoping activation of deformation mechanisms responsible for the soft-to-firm transition (Figure 2b), which qualitatively mimics the sequential unfolding, stretching, and yielding of microfibrils in collagen networks.[30]

To validate this concept, we synthesized two groups of LBL triblock copolymers with a polydimethylsiloxane (PDMS) bottlebrush block (B-block) and two poly(methyl methacrylate) (PMMA) linear end-blocks (L-blocks). These groups differ by the degree of polymerization (DP) of PDMS side chains, $n_{sc} = 14$ (Group 1) and $n_{sc} = 70$ (Group 2) and contain several series of LBL triblocks with different DP's of bottlebrush backbone (n_{bb} = 100−1100) and PMMA L-block (n_L = 50−1300) (Table S3). Figure 3a compares representative stress−elongation curves from each group to demonstrate the effects of n_L and n_{sc} on the Young's modulus and strain-stiffening (Figure S1 shows a complete set of deformation curves). An [E_0, β] map reveals that all Group 1 plastomers coalesce (green, Figure 3b) to successfully cross the gel-tissue divide, yet skirt many essential tissues such as muscle ($\beta = 0.7$), skin ($\beta = 0.8$), and fat ($\beta = 0.9$) located in the bottom-right corner of the tissue territory. To reach this corner, LBL's with longer side chains (Group 2) were employed. Elongating side chains simultaneously reduces cross-link density and extends network strands, thereby maintaining tissue-relevant softness with enhanced firmness that yields a shift in the observed coalescence (black symbols in Figure 3b).

https://dx.doi.org/10.1021/acscentsci.9b01216
ACS Cent. Sci. 2020, 6, 413−419

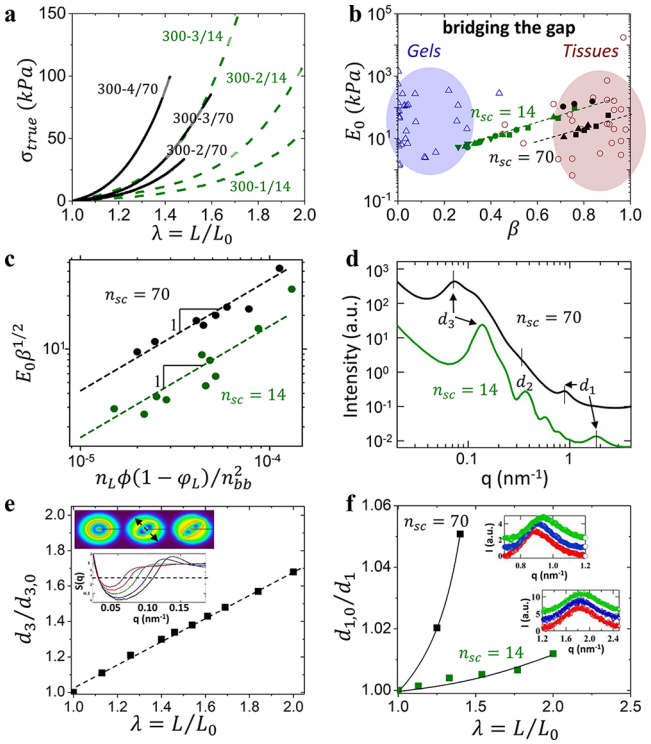

Figure 3. Bridging the gap. (a) Stress−elongation comparison of Group 1 (n_{sc} = 14, dashed) versus Group 2 (n_{sc} = 70, solid) plastomers with similar B-block backbone DP n_{bb} = 300 and L-block volume fraction ϕ_L = 0.3−0.9 demonstrate Group 2's enhanced strain-stiffening. (b) The E_0 vs β plot from Figure 1d where Group 1 plastomers (green) enable gel-tissue bridging, while Group 2 plastomers (black) successfully penetrate into the tissue territory (Tables S1−S3). Dashed lines are used to guide the reader and not indicative of theoretical correlation. Group 2 plastomers with shorter backbones (n_{bb} = 100) shift toward higher E_0 (black ●), due to a star-like strand conformation as $n_{bb} \approx n_{sc}$ (Figure S1). (c) Correlation between mechanical properties (E_0 and β) and molecular parameters (n_L, n_{bb}, ϕ_L) demonstrate good agreement with theoretical analysis summarized in eq S10, where $\phi = n_g/(n_g+n_{sc})$. (d) Selected USAXS/SAXS spectra of Group 1 and 2 plastomers with a similar $n_{bb} \cong 300$ (see Supporting Information for a complete set of X-ray curves for a complete set of X-ray curves). The observed increase of the interdomain spacing (d_3) of Group 2 plastomers correlates with enhanced strain-stiffening from longer side chains. (e) Uniaxial extension of a Group 1 plastomer results in a d_3 increase obtained from in situ variation of the structure factor $S(q)$ in the stretching direction (arrow in inset). $S(q)$ was computed by dividing the total scattering intensity by the fit of the form-factor of polydisperse solid spheres. The 2D USAXS patterns given in the inset correspond the to the values of λ of 1.0, 1.4, and 2.0 (from left to right). Azimuthal variations in the 2D USAXS pattern suggest network topology restructuring during deformation. (f) Relative decrease of the d_1 spacing during elongation was deduced from the high-q shifts of the bottlebrush peak (insets) with Group 2 plastomers exhibiting stronger dependence consistent with enhanced strand firmness.

Theoretical analysis (eqs S1−S10 and Figure 3c) corroborates the observed n_{sc}-specific coalescence in Figure 3b by correlating the attained mechanical properties with the corresponding architectural parameters (Figure 3c). For a fixed n_{sc}, this universality serves as a theoretical foundation for independently tailoring plastomer firmness from its softness. The architectural firmness enhancement is probed by ultra-small angle X-ray scattering (USAXS) at different length scales both before (Figure 3d) and during deformation (Figure 3e,f).[31] Prior to deformation, B-block filaments are self-extended due to strong microphase segregation evidenced by the well-defined microdomain size (d_2) and periodicity (d_3) (Figure 3d and Table S3). For a given ϕ_L and n_{bb}, an n_{sc} increase results in a (2.2 ± 0.2)× increase in $R_{in} \approx d_3 - D_L$ consistent with the enhanced firmness (β_{70}/β_{14} = 1.7 ± 0.1), where D_L is the diameter of PMMA spherical domains determined from their form-factor (d_2). During deformation, strand extension is a product of three mechanisms operating at different stresses (Figure 2b) evidenced by low-q shifts of the d_3 spacing (Figure 3e) and high-q shift of the d_1 spacing (Figure 3f). Even though the d_1 spacing is nontrivially related to bottlebrush block diameter,[32] the high-q shift is indicative of backbone extension given to the constant packing density constraint (condition). Because of a lower filament extension threshold of $\sim(k_BT)/R_{sc}$, Group 2 plastomers undergo backbone extension prior to yielding of linear block domains at $\sim\gamma_{LB}l_0$ (Figure 2b). This results in stronger dependence of d_1 on deformation of ca. 5% compared to 1% shown by Group 1 (Figure 3f). Although both variations are marginal with respect to the total strain of 50−100%, they cause significant force augmentation due to nonlinear elasticity of the pre-extended backbone.[8,9] In addition to unraveling of bottlebrush strands and backbone extension, a d_3 shift includes withdrawal of linear blocks from the L-domains. Even though X-ray measurements did not give measurable evidence of linear block withdrawal due to its small effect on d_2, microdomain yielding was corroborated by measuring loading−unloading hysteresis as a function of deformation (Figure S2) and by computer simulations of plastomer deformation.[17] Despite microdomains yielding, deformation of plastomer samples was fully reversible up to rupture, whereas an onset of hysteresis was observed at $\lambda \approx 0.6\lambda_{max}$. At elongations $\lambda < 0.6\lambda_{max}$, plastomers demonstrate elastic deformation without hysteresis ascribed to extension of network strands.

Regulating firmness (β) without compromising softness (E_0) has significant implications in the design of biomedical devices and is particularly challenging for ultrasoft and ultrafirm tissues. Figure 4a exemplifies stress−elongation curves of assorted plastomers that reveal agreeable mechanical responses with brain, fetal membrane, and spinal cord tissues. These solvent-free materials also successfully replicate adipose tissues (Figure 4b) and serve as a superior solution to commercially available silicone gel-based products (Figure 1c) that leach into the body.[15,16] Additionally, biological tissues exhibit significant variation in mechanical response depending on bodily location, age, strain rate, and deformation direction with respect to tissue texture. In the Supporting Information, we demonstrate additional tunability potential of the plastomer platform by mixing LBL plastomer networks with corresponding LB diblocks and free bottlebrushes (Figure S3). Although LBL plastomers precisely replicate most of the stress−strain response of biological tissue including the initial elasticity and subsequent yielding, they fall short of mimicking tissue strength at rupture and represent one of the challenges for future studies.

The LBL platform also exhibits adequate biocompatibility as demonstrated by the adhesion and proliferation of human normal mammary epithelial and adipose-derived mesenchymal stem cells (MSCs) cultured onto a 300−1/70 surface (Figure 4c). Monitoring the cultured cells by fluorescence microscopy over the course of a week reveals plastomers as adequate substrates for both cell's viability and proliferation (Figure

https://dx.doi.org/10.1021/acscentsci.9b01216
ACS Cent. Sci. 2020, 6, 413−419

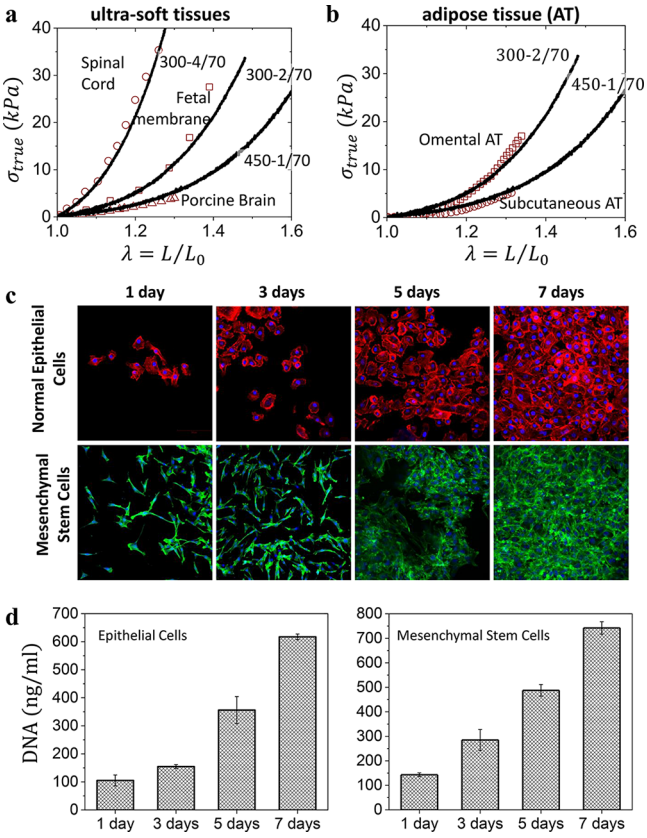

Figure 4. Plastomer tissue relevance and biocompatibility. (a) Selected true stress−elongation curves of Group 2 plastomers (lines) overlaid onto spinal cord, fetal membrane, and porcine brain tissues (symbols) found in the literature (Table S1) with similar mechanical properties. (b) Selected true stress−elongation curves of Group 2 plastomers (lines) match different types of adipose tissue (symbols). (c) The proliferation of human normal mammary epithelial and adipose-derived mesenchymal stem cells cultured onto a 300−1/70 plastomer surface and monitored by fluorescence microscopy after 1, 3, 5, and 7 days. Cells became confluent within 7 days. (d) Corresponding DNA quantification of the cultured human normal mammary epithelial and adipose-derived mesenchymal stem cells after 1, 3, 5, and 7 days.

4c,d). In contrast, silicone gels used in commercial breast implants show a high cytotoxicity likely due to leaching of an ill-defined liquid fraction poisoning cells. We quantified the leachability via aqueous extraction of the sol fraction from both a commercial silicone gel and our plastomer over 1 month (Figure S4), which highlights the higher purity of plastomers as compared with current leading commercial products.

CONCLUSION

This study has significantly advanced our understanding of the materials design platform previously reported[17] by (i) elucidating the material's deformation mechanism encoded into a single network strand and (ii) demonstrating that our materials not only bridge the firmness divide between traditional soft gels and tissues, but have also successfully replicated the evolutionary soft-to-firm mechanical response found in particularly soft brain, fetal membrane, and fat tissues. Furthermore, these solvent-free materials exhibit superior biocompatibility compared with commercial products and show promise for further in vivo studies. We believe combining these unique characteristics will revolutionize future applications in the emerging biomedical and soft-robotics fields.

EXPERIMENTAL SECTION

Materials. Methyl methacrylate (MMA, 99%) was obtained from Thermo Fisher Scientific and purified using a basic alumina column to remove inhibitor. Tetrahydrofuran (THF), anisole, toluene, acetone, and isopropanol were purchased from Fisher Scientific and used as received. Monomethacryloxypropyl-terminated poly(dimethylsiloxane) (MCR-M17, M_n = 5000 g/mol, DP = 70, $Đ$ = 1.15) was obtained from Gelest and purified using basic alumina columns to remove inhibitor. Copper(I) bromide (CuBr, 99.999%), tris[2-(dimethylamino)-ethyl]amine (Me_6TREN), and ethylene bis(2-bromoisobutyrate) (2-BiB, 97%) were purchased from Sigma-Aldrich and used as received.

No unexpected or unusually high safety hazards were encountered.

Synthesis of Poly(dimethylsiloxane) Bottlebrushes. Synthetic procedures are similar to previously reported linear−brush−linear plastomers.[17] A 100 mL Schlenk flask equipped with a stir bar was charged with 2-BiB (9.6 mg, 26.6 μmol), MCR-M17 (50.0 g, 10 mmol), Me_6TREN (12.2 mg, 14.2 μL, 53.3 μmol), and a solvent mixture of anisole (40 mL) and toluene (10 mL). The solution was bubbled with dry nitrogen for 1.5 h, and then Cu(I)Br (7.6 mg, 53.3 μmol) was quickly added to the reaction mixture under nitrogen atmosphere. The flask was sealed, purged for an additional 15 min, and then immersed in a 45 °C oil bath. The polymerization was stopped after 5 h to yield 79% monomer conversion as verified by ^{1}H NMR (Figures S5 and S6), resulting in a bottlebrush PDMS polymer with DP of the backbone (n_{bb}) ≈ 300. The polymer was precipitated two to three times from isopropanol to purify residual macromonomers. The resulting purified polymer was dried under a vacuum at room temperature until a constant mass was reached.

Linear−Bottlebrush−Linear ABA Plastomer Synthesis and Film Preparation. The resulting PDMS bottlebrushes were used as bifunctional ATRP macroinitiators to grow PMMA at both ends using a similar procedure. For example, PDMS marco-initiator (5 g, 3.37 μmol), excess MMA (1 g), and Me_6TREN (1.5 g, 1.8 μL, 6.75 μmol) were dissolved in a mixture of anisole (5 mL) and toluene (10 mL), degassed and followed with the addition of Cu(I)Br (0.96 g, 6.75 μmol). Growth of linear MMA was monitored by ^{1}H NMR, and samples were quenched to afford a series of ABA block copolymers with an increasing linear-to-bottlebrush ratio. The resulting products were swelled and washed two to three times with acetone to remove MMA homopolymer and then swelled and washed two to three times with hexanes to remove unreacted PDMS bottlebrush and dried overnight (Figure S5). A full synthetic inquiry into these impurities will be the subject of a later publication. Finally, the DP and volume fraction of linear end bocks were measured by ^{1}H NMR (Figure S7) as summarized in Table S3. Samples were dissolved in 85 wt % THF and cast into Teflon Petri-dishes (Welch Fluorocarbon) and left to dry overnight.

Atomic Force Microscopy. The imaging was performed in PeakForce QNM mode using a multimode AFM (Brüker) with a NanoScope V controller and silicon probes (resonance frequency of 50−90 Hz and spring constant of ~0.4 N/m). Bottlebrush B block dimensions are extracted from AFM

https://dx.doi.org/10.1021/acscentsci.9b01216
ACS Cent. Sci. 2020, 6, 413−419

images in Figure S8 and are consistent with expected dimensions described by ^{1}H NMR.

Small- and Ultrasmall-Angle X-ray Scattering (SAXS and USAXS). The USAXS and SAXS measurements (Figure S9 and Table S3) were carried out at the ID02 beamline of the European Synchrotron Radiation Facility (ESRF) in Grenoble, France. The experiments were conducted in transmission geometry using a photon energy of 12.46 keV. The recorded 2D data were centered, calibrated, regrouped, and reduced to 1D using the SAXS utilities platform described elsewhere.[33] The analysis of the SAXS and USAXS data was performed using the SANS & USANS data reduction and analysis package provided by NIST[34] for the Igor Pro environment (WaveMetrics Ltd.).

The monochromatic incident X-ray beam was collimated on the sample to a footprint of 100 × 200 μm^2 ($V \times H$). The total photon flux was estimated to be 9×10^{11} ph/s allowing for acquisition times of less than 100 ms. The accessed q values, with $|q| = 4\pi \sin(\theta)/\lambda$, where θ is the Bragg angle and λ is the wavelength, cover a range from 7.0×10^{-3} nm^{-1} to 5.0 nm^{-1}. A Rayonix MX-170HS implemented in a 35 m long vacuum flight tube was applied for recording of SAXS and USAXS intensities at two different sample-to-detector distances of 1.5 and 10.0 m, respectively. For optimization of the scattering signal, a binning of 2 × 2 pixels was applied resulting in an effective pixel size of 89 μm in both directions.

The in situ mechanical and structural measurements were performed with the help of a custom-made stretching device compatible with the ID02 beamline environment. The stretching device allowed for computer controlled synchronized motion of the two symmetrical fixtures in which the dog bone-shaped sample was clamped. For each deformation, the position of the X-ray beam on the sample was refined by scanning it along two perpendicular directions. The structural irreversibility in the loading/unloading cycles in the linear regime was specifically checked and found negligible for all the samples studied.

For quantitative analysis of the USAXS−SAXS curves, we utilize the scattering intensity as $I(q) \approx \Phi^2(q)S(q)$ where $S(q)$ is the structure factor and $\Phi(q)$ is the form-factor, which, for homogeneous monodisperse spheres, has the following form $\Phi(q) = \frac{3}{(qR)^3}[\sin(qR) - qR\cos(qR)]$. The polydispersity effect was incorporated by a convolution of the scattering intensity with the Gaussian size distribution functions. After extracting the PMMA sphere diameter (D_L) and its polydispersity, the $S(q)$ functions were analyzed.

Uniaxial Tensile Stress Strain Measurements. Dog bone-shaped samples with bridge dimensions of 12 mm × 2 mm × 1 mm were loaded into an RSA-G2 DMA (TA Instruments) and subjected to uniaxial extension at 20 °C and constant strain rate of 0.005 s^{-1}. Samples were stretched until rupture, revealing the entire mechanical profile. In each case, tests were conducted in triplicate to ensure accuracy of the data. All stress−elongationcurves show dependence of the true stress σ_{true} on the elongation ratio λ in accordance with eq 1 at small and intermediate deformation range but switch to a linear scaling with λ at the later stages of deformation (Figure S1 and Table S3). The elongation ratio λ for uniaxial network deformation is defined as the ratio of the sample's instantaneous size L to its initial size L_0, $\lambda = L/L_0$.

Biological Characterization of Tissue-like Substrates. To prepare substrates for cell culture study, tissue-like substrates were placed in a 24-well plate, and type-1 collagen was conjugated to their surface using the heterobifunctional linker *N*-sulfosuccinimidyl-6-(4′-azido-2′-nitrophenylamino) hexanoate (sulfo-SANPAH, Pierce). In brief, 500 μL of a 0.2 mg/mL solution of sulfo-SANPAH in milli-Q H_2O was added to each well in a 24-well plate which was then placed under a 365 nm UV light, and irradiated for 5 min. Subsequently, the substrates were washed three times with 50 mM HEPES in PBS. Afterward, 500 μL of 50 μg/mL type-1 collagen was added to each well, and the plate was stored 3 h at 4 °C to prevent collagen polymerization but allow the collagen to react to the surface. The collagen coated tissue-like substrates were washed three times with PBS and then incubated with culture media, 10% fetal bovine serum with 1% pen-strep in Dulbecco's modified Eagle medium warmed to 37 °C.

Two cell types of human normal mammary epithelial cells and adipose-derived mesenchymal stem cells were used for biological characterization of tissue-like substrates. Trypsinzed cells were seeded on the collagen functionalized substrates at an initial concentration of 20 000/cm^2. Cell proliferation was analyzed over a week, while culture media was changed twice. To quantify the cellular proliferation on the substrate in the course of 1 week, the DNA content of the cells was measured using the Quanti-iT PicoGreen dsDNA kit (Invitrogen, USA) according to the manufacturer's instructions. Fluorescence microscopy was also measured to monitor the cells over a week. Immunohistochemical staining was performed using Cytopainter Red Fluorescence F-actin Staining kit and Cytopainter Green Fluorescence F-actin Staining kit for epithelial and mesenchymal stem cells, respectively, following the manufacturer's instructions. The 4′,6-diamidino-2-phenylindole (DAPI) was used to stain cell nuclei.

■ ASSOCIATED CONTENT

Supporting Information

The Supporting Information is available free of charge at https://pubs.acs.org/doi/10.1021/acscentsci.9b01216.

Theoretical discussion of LBL plastomer structure and elastic properties, mechanical parameters of literature tissues and gels, structural and mechanical properties of LBL plastomers from ^{1}H NMR, AFM, X-ray and stress−elongation curves, and leachability tests of samples (PDF)

■ AUTHOR INFORMATION

Corresponding Authors

Dimitri A. Ivanov − *Institut de Sciences des Matériaux de Mulhouse-IS2M, Mulhouse F-68057, France; Faculty of Fundamental Physical and Chemical Engineering, Lomonosov Moscow State University, Moscow 119991, Russian Federation; Institute of Problems of Chemical Physics, Russian Academy of Sciences, Chernogolovka 142432, Russian Federation*; Email: dimitri.ivanov@uha.fr

Andrey V. Dobrynin − *Department of Polymer Science, University of Akron, Akron, Ohio 44325-3909, United States;* orcid.org/0000-0002-6484-7409; Email: adobrynin@uakron.edu

Sergei S. Sheiko − *Department of Chemistry, University of North Carolina at Chapel Hill, Chapel Hill, North Carolina 27599, United States;* orcid.org/0000-0003-3672-1611; Email: sergei@email.unc.edu

https://dx.doi.org/10.1021/acscentsci.9b01216
ACS Cent. Sci. 2020, 6, 413−419

Other Authors

Andrew N. Keith − *Department of Chemistry, University of North Carolina at Chapel Hill, Chapel Hill, North Carolina 27599, United States*

Mohammad Vatankhah-Varnosfaderani − *Department of Chemistry, University of North Carolina at Chapel Hill, Chapel Hill, North Carolina 27599, United States*

Charles Clair − *Laboratoire de Physique et Mécanique Textiles, Université de Haute Alsace, Mulhouse F-68093, France*

Farahnaz Fahimipour − *Department of Chemistry, University of North Carolina at Chapel Hill, Chapel Hill, North Carolina 27599, United States*

Erfan Dashtimoghadam − *Department of Chemistry, University of North Carolina at Chapel Hill, Chapel Hill, North Carolina 27599, United States*

Abdelaziz Lallam − *Laboratoire de Physique et Mécanique Textiles, Université de Haute Alsace, Mulhouse F-68093, France*

Michael Sztucki − *European Synchrotron Radiation Facility, Grenoble F-38043, France*

Heyi Liang − *Department of Polymer Science, University of Akron, Akron, Ohio 44325-3909, United States;* orcid.org/0000-0002-8308-3547

Complete contact information is available at: https://pubs.acs.org/10.1021/acscentsci.9b01216

Author Contributions

A.N.K. and M.V.V. designed, synthesized, and characterized the monomers, block copolymers, and polymer networks; A.N.K. performed mechanical tests and AFM experiments. H.L. and A.V.D. provided theoretical analysis of mechanical properties, developed theoretical foundation for materials design and LBL networks; C.C., A.L., M.S., and D.A.I. conducted X-ray studies and data analysis; F.F. and E.D. contributed to methodology, biological assays, and mechanical tests; S.S.S. was the principal investigator, A.N.K. and S.S.S were primary writers of the manuscript. All authors discussed the results and provided feedback on the manuscript.

Notes

The authors declare no competing financial interest.

■ ACKNOWLEDGMENTS

We acknowledge funding from the National Science Foundation (DMR 1407645, DMR 1921835, and DMR 1921923). S.S. acknowledges financial support from the Ministry of Education of the Russian Federation within State Contract No. 14.W03.31.0022. D.A.I. declares that this work was performed in accordance with the state task No. AAAA-A19-119101590029-0.

■ REFERENCES

(1) Blair, G. W. S. A new criterion for expressing the 'intensity of firmness' of soft bodies. *Nature* **1943**, *152*, 412.

(2) Faber, T. J.; Jaishankar, A.; McKinley, G. H. Describing the firmness, springiness and rubberiness of food gels using fractional calculus. Part I: Theoretical framework. *Food Hydrocolloids* **2017**, *62*, 311−324.

(3) Fung, Y. C. *Biomechanics: Mechanical Properties of Living Tissues*, 2nd ed.; Springer, 1993.

(4) Holzapfel, G. A. Biomechanics of soft tissue. In *Handbook of Material Behavior Models*, 1st ed.; LeMaitre, J., Eds.; Academic Press, 2001; pp 1057−1071.

(5) Storm, C.; Pastore, J. J.; MacKintosh, F. C.; Lubensky, T. C.; Janmey, P. A. Nonlinear elasticity in biological gels. *Nature* **2005**, *435*, 191−194.

(6) Carrillo, J.-M. Y.; MacKintosh, F. C.; Dobrynin, A. V. Nonlinear elasticity: from single chain to networks and gels. *Macromolecules* **2013**, *46*, 3679−3692.

(7) Whitesides, G. M. Soft robotics. *Angew. Chem., Int. Ed.* **2018**, *57*, 4258−4273.

(8) Xu, K.; Lu, Y.; Takei, K. Multifunctional skin-inspired flexible sensor systems for wearable electronics. *Adv. Mater. Technol.* **2019**, *4*, 1800628.

(9) Peters, W.; Brandon, H.; Jerina, K. L.; Wolf, C.; Young, V. L. In *Biomaterials in Plastic Surgery. Breast Implants*; Woodhead Publishing, 2012.

(10) Jeong, J.-W.; Shin, G.; Park, S. I.; Yu, K. J.; Xu, L.; Rogers, J. A. Soft materials in neuroengineering for hard problems in neuroscience. *Neuron* **2015**, *86*, 175−186.

(11) Scholten, K.; Meng, E. Materials for microfabricated implantable devices: A review. *Lab Chip* **2015**, *15*, 4256−4272.

(12) Teo, A. J. T.; Mishra, A.; Park, I.; Kim, Y.-J.; Park, W.-T.; Yoon, Y.-J. Polymeric biomaterials for medical implants and devices. *ACS Biomater. Sci. Eng.* **2016**, *2*, 454−472.

(13) Feig, V. R.; Tran, H.; Lee, M.; Bao, Z. Mechanically tunable conductive interpenetrating network hydrogels that mimic the elastic moduli of biological tissue. *Nat. Commun.* **2018**, *9*, 2740.

(14) Li, Y.; Sariyer, O. S.; Ramachandran, A.; Panyukov, S.; Rubinstein, M.; Kumacheva, E. Universal behavior of hydrogels confined to narrow capillaries. *Sci. Rep.* **2015**, *5*, 17017.

(15) Yu, L. T.; Latorre, G.; Marotta, J.; Batich, C.; Hardt, N. S. In vitro measurement of silicone bleed from breast implants. *Plast. Reconstr. Surg.* **1996**, *97*, 756−764.

(16) Coroneos, C. J.; Selber, J. C.; Offodile, A. C.; Butler, C. E.; Clemens, M. W. US FDA breast implant postapproval studies: long-term outcomes in 99,993 patients. *Ann. Surg.* **2019**, *269*, 30−36.

(17) Vatankhah-Varnosfaderani, M.; Keith, A. N.; Cong, Y.; Liang, H.; Rosenthal, M.; Sztucki, M.; Clair, C.; Magonov, S.; Ivanov, D. A.; Dobrynin, A. V.; Sheiko, S. S. Chameleon-like elastomers with molecularly encoded strain-adaptive stiffening and coloration. *Science* **2018**, *359*, 1509−1513.

(18) Vatankhah-Varnosfaderani, M.; Daniel, W. F. M.; Everhart, M. H.; Pandya, A. A.; Liang, H.; Matyjaszewski, K.; Dobrynin, A. V.; Sheiko, S. S. Mimicking biological stress-strain behavior with synthetic elastomers. *Nature* **2017**, *549*, 497−501.

(19) Dobrynin, A. V.; Carrillo, J. Y. Universality in nonlinear elasticity of biological and polymeric networks and gels. *Macromolecules* **2011**, *44*, 140−146.

(20) Jacobs, M.; Liang, H.; Dashtimoghadam, E.; Morgan, B. J.; Sheiko, S. S.; Dobrynin, A. V. Nonlinear Elasticity and Swelling of Comb and Bottlebrush Networks. *Macromolecules* **2019**, *52*, 5095−5101.

(21) Gong, J. P.; Katsuyama, Y.; Kurokawa, T.; Osada, Y. Double-network hydrogels with extremely high mechanical strength. *Adv. Mater.* **2003**, *15*, 1155−1158.

(22) Chen, Q.; Liang, S.; Thouas, G. A. Elastomeric biomaterials for tissue engineering. *Prog. Polym. Sci.* **2013**, *38*, 584−671.

(23) Ducrot, E.; Chen, Y.; Bulters, M.; Sijbesma, R. P.; Creton, C. Toughening elastomers with sacrificial bonds and watching them break. *Science* **2014**, *344*, 186−189.

(24) Wang, Z.; Jiang, F.; Zhang, Y.; You, Y.; Wang, Z.; Guan, Z. Bioinspired design of nanostructured elastomers with cross-linked soft matrix grafting on the oriented rigid nanofibers to mimic mechanical properties of human skin. *ACS Nano* **2015**, *9*, 271−278.

(25) Jaspers, M.; Vaessen, S. L.; van Schayik, P.; Voerman, D.; Rowan, A. E.; Kouwer, P. H. J. Nonlinear mechanics of hybrid polymer networks that mimic the complex mechanical environment of cells. *Nat. Commun.* **2017**, *8*, 15478.

(26) So, J.-H.; Tayi, A. S.; Güder, F.; Whitesides, G. M. Stepped moduli in layered composites. *Adv. Funct. Mater.* **2014**, *24*, 7197−7204.

(27) Sheiko, S. S.; Dobrynin, A. V. Architectural code for rubber elasticity: from Super-soft to super-firm materials. *Macromolecules* **2019**, *52*, 7531−7546.
(28) Ohta, T.; Kawasaki, K. Equilibrium morphology of block copolymer melts. *Macromolecules* **1986**, *19*, 2621−2632.
(29) Fantner, G. E.; Oroudjev, E.; Schitter, G.; Golde, L. S.; Thurner, P.; Finch, M. M.; Turner, P.; Gutsmann, T.; Morse, D. E.; Hansma, H.; Hansma, P. K. Sacrificial bonds and hidden length: unraveling molecular mesostructures in tough materials. *Biophys. J.* **2006**, *90*, 1411−1418.
(30) Depalle, B.; Qin, Z.; Shefelbine, S. J.; Buehler, M. J. Influence of cross-link structure, density and mechanical properties in the mesoscale deformation mechanisms of collagen fibrils. *J. Mech. Behav. Biomed Mater.* **2015**, *52*, 1−13.
(31) Clair, C.; Lallam, A.; Rosenthal, M.; Sztucki, M.; Vatankhah-Varnosfaderani, M.; Keith, A. N.; Cong, Y.; Liang, H.; Dobrynin, A. V.; Sheiko, S. S.; Ivanov, D. A. Strained bottlebrushes in super-soft physical networks. *ACS Macro Lett.* **2019**, *8*, 530−534.
(32) Liang, H.; Wang, Z.; Dobrynin, A. V. Scattering from melts of combs and bottlebrushes: molecular dynamics simulations and theoretical study. *Macromolecules* **2019**, *52*, 5555−5562.
(33) Sztucki, M.; Narayanan, T. Development of an ultra-small-angle x-ray scattering instrument for probing the microstructure and the dynamics of soft matter. *J. Appl. Crystallogr.* **2007**, *40*, 459−462.
(34) Kline, S. R. Reduction and analysis of SANS and USANS data using IGOR Pro. *J. Appl. Crystallogr.* **2006**, *39*, 895−900.

https://dx.doi.org/10.1021/acscentsci.9b01216
ACS Cent. Sci. 2020, 6, 413−419